TECHNICAL & APPLIED ARTICLE

OPEN ACCESS

Radiation of higher order modes from circular ducts with flow

Courtney Ford[*] ⓘ, Antonio Pereira ⓘ, and Christophe Bailly ⓘ

Univ Lyon, Ecole Centrale de Lyon, CNRS, Univ Claude Bernard Lyon 1, INSA Lyon, LMFA, UMR5509, 69130 Ecully, France

Abstract – This work aims to predict the transfer function of a given modal content inside a circular duct with a bellmouth inlet in the presence of a mean flow. The transfer function is the relation in amplitude and phase between a given mode inside the duct and an observer located in the far-field. The numerical solution is obtained by finite element simulation in which the mean flow is input data. Verification is provided by comparison to the analytical solution of an unbaffled circular duct with uniform flow. Influence from various parameters such as the geometry and mean Mach number on the radiated pressure field is investigated. The analytical solution is a good approximation for finding the radiated principal lobe, and the inlet geometry is found to be more important than other parameters such as mean flow when static inlet configuration is studied.

Keywords: Modal radiation, Unflanged circular duct, Static inlet configuration, Transfer function

1 Introduction

The field of duct acoustics began with the work by Lord Rayleigh [1] on the theory of sound. He considered noise moving through many different duct types, including circular conduits and both flanged and unflanged ducts. Levine and Schwinger [2] produced the analytical solution for the specific case of a plane wave propagating in and radiating out from an unflanged, axisymmetric, circular pipe. Subsequent work was undertaken by Weinstein [3], who extended Levine and Schwinger's analytical work to include higher order modes, focusing on adapting the Wiener–Hopf technique to be applied to acoustic modes in circular waveguides. Tyler and Sofrin [4] conducted experimental work mapping the pressure fields produced by ducts with bellmouth inlets with the specific goal of reducing the noise produced by aircraft engines. This pair then went on to consider unbaffled ducts in a simplified study that neglected some physical properties, such as diffraction effects from the duct edges.

Candel [5, 6] added diffraction effects on blunt leading and trailing edges and considered the effects of a uniform flow everywhere, a flow condition that exists naturally a few miles after take-off or before landing with reduced power, when the aircraft and exhaust gases have the same velocity. Lordi et al. [7, 8] considered an infinitely-long annular duct with a uniform throughflow, then extended their work to include a rotor positioned a finite distance from the end of an unflanged, semi-infinite duct. Like

Candel, they took the diffraction into account, this time for a sharp leading edge which drastically changed the acoustic far-field field measured behind and to the side of the duct. They also found that the propagating angle of the wave fronts with respect to the duct axis is important because it determines the location of the peak of the principal lobe in the far-field radiation. Rice et al. [9] derived simple expressions for these angles that are valid near the duct outer wall (the most important region in duct acoustics). They considered multiple flow conditions, including uniform steady flow, zero Mach number in the far-field with steady flow in the duct, and increasing Mach number in the far-field. It was determined that the angle of propagation with respect to the z-axis is identical to the angle of the peak of the principal lobe of far-field radiation both with and without flow. Additionally, they found that as Mach number increases, this angle shifts away from the z-axis. Not considered was refraction of the sound by flow gradients near the inlet. Snakowska et al. [10] compared experimental and analytical far-field pressure solutions for a semi-infinite unflanged circular duct with harmonic, axisymmetric excitations, and Lidoine [11, 12] drew from these sources to produce a general analytical code for such a model. This was one of the models used by Guerin [13] to study the behavior of normally-evanescent pressure waves in ducts with very short nacelles. He considered a circular duct with uniform axial flow and found that cut-off modes will propagate if the engine nacelle is sufficiently short.

In order to reconstruct modal content inside a duct from pressure measurements made externally using an iterative Bayesian inverse approach, it is necessary to derive a

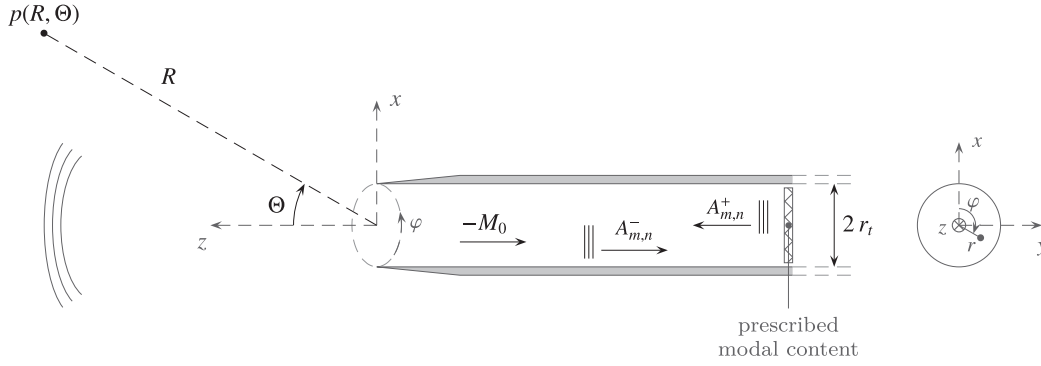*Corresponding author: courford@gmail.com,
courtney.ford@ec-lyon.fr

Figure 1. Sketch of the configuration and used notation.

working transfer function [14]. This inverse problem can be solved numerically with finite element simulations for external arrays with geometries that are too complex for analysis, and verified by comparison with analytical reconstructions from pressure measurements taken using an internal array. The software Actran is employed for numerical simulations and an in-house analytical code based on the Wiener–Hopf technique is developed and verified with an external code created by Rienstra [15], which was very recently made available online [16]. First, the software is validated by comparison with the analytical code for a simple case of an unflanged circular duct with a beveled edge. The importance of various parameters is tested, such as duct wall thickness and the edge angle. Next, directivity plots are generated to compare the far-field pressure for a complex-geometry inlet to the analytical and numerical fields. Various flow fields are tested and the differences in their generation and results are analyzed. By validating the transfer matrices produced by the software, it can later be used to derive matrices for more complex systems and validate experimental research.

The analytical code and its verification are discussed in Section 2, the numerical simulations are introduced in Section 3, the simulation without flow is presented in Section 4, several simulations with flow are included in Section 5, and simulations of the geometry of an experimental test rig are studied in Section 6.

2 Analytical model

The inlet of a three-dimensional circular duct of diameter $2r_t$ with narrow solid walls is considered, as shown in Figure 1. Modal forcing is imposed inside the duct to mimic the presence of a blade row, and a mean flow is also included; the Mach number associated with the bulk velocity inside the duct is denoted M_0. The acoustic radiated field is computed for an observer located at (R, Θ) in the far-field. Spherical coordinates are introduced outside where R is the radial distance, Θ the polar angle, and φ the azimuthal angle. The origin of the frame is taken at the duct inlet, and the sound field is expected to be symmetric with respect to φ.

2.1 Analytical solution

The acoustic field inside an infinite rigid duct can be expressed as a decomposition of orthogonal modes. Using cylindrical coordinates (z, r, φ), we get,

$$p(z, r, \varphi) = \sum_{m=-\infty}^{+\infty} \sum_{n=0}^{+\infty} \left[A_{m,n}^+ e^{i\tilde{k}_{z_{m,n}}\tilde{z}} \right.$$
$$\left. + A_{m,n}^- e^{-i\tilde{k}_{z_{m,n}}\tilde{z}} \right] f_{m,n}(r) e^{i(m\varphi - M_0 \tilde{k}_0 \tilde{z})}, \tag{1}$$

where m and n denote the azimuthal and radial mode indices respectively and $A_{m,n}^+$ and $A_{m,n}^-$ are the complex amplitudes of the propagating modes. Their superscripts $+$ and $-$ refer to the direction of propagation, downstream or upstream with respect to the z-axis. The radial mode shape $f_{m,n}$ is usually normalized due to an inner scalar product [17] and the presence of a subsonic mean flow is taken into account with the Prandtl–Glauert transformation [6, 18]. The axial coordinate has been normalized by the Prandtl–Glauert factor $\beta = \left(1 - M_0^2\right)^{1/2}$ leading to $\tilde{z} = z/\beta$ and $\tilde{k}_0$ is the normalized acoustic wave number, defined by $\tilde{k}_0 = k_0/\beta = (\omega/c_0)/\beta$ with ω the angular frequency and c_0 the speed of sound. The dispersion relation of acoustic waves can be recast as follows for the normalized axial wave number $\tilde{\kappa}_{z_{m,n}} = \kappa_{z_{m,n}}/\beta$,

$$\beta^2 \tilde{\kappa}_{z_{m,n}} = -M_0 \tilde{k}_0 + \tilde{k}_{z_{m,n}} \qquad \tilde{k}_{z_{m,n}} = \sqrt{\tilde{k}_0^2 - \tilde{k}_{r_{m,n}}^2}. \tag{2}$$

As shown in Figure 2, the axial wave number $\tilde{\kappa}_{z_{m,n}}$ provides the effective propagation of the considered acoustic mode in presence of the mean flow. The effective angle of propagation is given with the expression,

$$\cos(\chi_{mn}) = \frac{\kappa_{z_{m,n}}^+}{\sqrt{\kappa_{z_{m,n}}^{+2} + k_{r_{m,n}}^2}}. \tag{3}$$

When M_0 increases, χ_{mn} also increases, leading to the maximum of the principal lobe shifting aftwards [9].

The normalized radial wavenumber $\tilde{k}_{r_{m,n}} = k_{r_{m,n}}/\beta$ is found by solving a boundary value problem (e.g. $k_{r_{m,n}} = \lambda_{m,n}/r_t$ for a circular duct where $\lambda_{m,n}$ is the n-th root
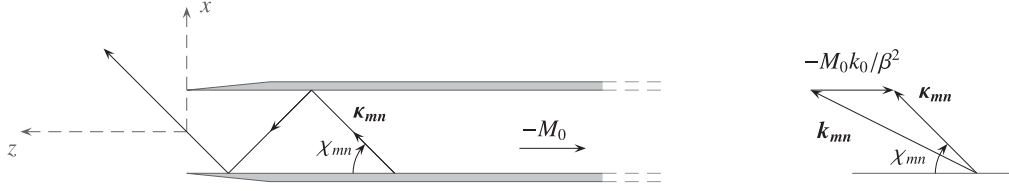
Figure 2. Illustration of the ray tracing for modal propagation.

of the derivative of the Bessel function J_m of the first kind of order m). In Expression (1), the sum over n is limited to the n_p propagating modes for a given spinning mode order m, that is when $\tilde{k}_0^2 - k_{r_{m,n}}^2 > 0$. In other words, n_p is the highest radial propagating mode.

The analytic solution for a finite-length duct was first formulated by Lordi et al. [7] and Homicz and Lordi [8] using the Wiener–Hopf technique to determine reflection coefficients for each mode at the inlet. This solution has been examined and generalized by Lidoine [11, 12] to include the presence of a mean flow still using the Prandtl–Glauert transformation. The approximate pressure field reads,

See the Equation (4) *bottom of the page*

The auxiliary phase function $\mathbf{\Omega}_m$ is defined as,

$$\Omega_m(\xi) = \tan^{-1}\left[\frac{Y'_m(\xi)}{J'_m(\xi)}\right] \pm \frac{\pi}{2}, \tag{5}$$

where the sign $+$ must be used for $m = 0$, and the sign $-$ otherwise. J_m is the m-th order Bessel function of the first kind and Y_m is the Bessel function of the second kind.

The numerical implementation of this solution requires a significant effort, as discussed in Lidoine [11, 12] and Ingenito [19]. This is especially due to the computation of the $\mathbb{S}$ function, that involves complex integrals. The function $\mathbb{S}(\xi)$ is defined as,

$$\mathbb{S}(\xi) = \frac{1}{\pi}\oint_{-\tilde{k}_0}^{\tilde{k}_0} \frac{\Omega_m\left(r_t\sqrt{\tilde{k}_0^2 - u^2}\right)}{u - \xi}\,\mathrm{d}u \pm i\Omega_m\left(r_t\sqrt{\tilde{k}_0^2 - \xi^2}\right)$$
$$+ \sum_{s=n_p+1}^{\infty} \ln\left[\frac{\tilde{k}_{z_{m,s}} + \xi}{\tilde{k}_{z_{m,s}} - \xi}\right] - \frac{1}{\pi}\int_{-i\infty}^{i\infty} \frac{\Omega_m\left(r_t\sqrt{\tilde{k}_0^2 - u^2}\right)}{u - \xi}\,\mathrm{d}u. \tag{6}$$

This equation is discussed in further detail in the Appendix.

Table 1. Table containing values used in the present simulations. Starred values (*) correspond to the LP3 testbench.

Variable	Notation	Value
Duct radius	r_t	0.085 m*
Distance from duct lip	R	1 or 2 m or 17.5 or 35 wavelengths
Evaluation frequency	f	6000 Hz
Azimuthal order	m	$0 - m_p$
Radial order	n	$0 - n_p$
Mach number	M_0	0, 0.12*, 0.30, 0.44
Velocity	U_0	0, 40*, 100, 150 m/s
Helmholtz number	H_e	9.42

2.2 Analytical implementation

Using the aforementioned techniques, an in-house code was developed with Matlab to determine acoustic pressure at a certain radial distance from the lip of a three-dimensional, thin-walled, circular, unbaffled duct. This code was designed to take higher order modes into account and was employed to produce directivity plots of the pressure around a conduit inlet.

Values for the requisite input variables are listed in Table 1: r_t was selected to match the radius of the LP3 engine [20] that will be used for experiments related to this work, R was chosen to be at several wavelengths distance from the duct so as to assure that it is outside of the near-field. f was determined to contain several higher order modes, m_p is the maximum propagating azimuthal order within the duct, and n_p represents the maximum propagating radial order within the duct for a given m. The four velocities were chosen to test the case without flow, maximum flow velocity in the LP3 engine [20] (Mach 0.12), and two higher velocities. The corresponding dimensionless Helmholtz number [21] is determined as follows,

$$H_e = kr_t = \frac{\omega}{c}r_t = \frac{2\pi f}{c}r_t. \tag{7}$$

$$p(R, \Theta) \approx A_{m,n}^+ \left[\frac{-J_m(k_{r_{m,n}}r_t)\tilde{k}_{z_{m,n}}}{\tilde{k}_0\cos(\Theta) - \tilde{k}_{z_{m,n}}}\sqrt{\frac{r_t^2 k_{r_{m,n}}^2 - m^2}{\pi k_{r_{m,n}}^2}}\sin\left[\Omega_m(\tilde{k}_0 r_t \sin\Theta)\right] \prod_{s=1, s\neq n}^{n_p}\left(\frac{\tilde{k}_{z_{m,s}} + \tilde{k}_{z_{m,n}}}{\tilde{k}_{z_{m,s}} - \tilde{k}_{z_{m,n}}}\right)\right]$$

$$\sqrt{\prod_{s=1}^{n_p}\left(\frac{\tilde{k}_{z_{m,s}} - \tilde{k}_0\cos\Theta}{\tilde{k}_{z_{m,s}} + \tilde{k}_0\cos\Theta}\right)} e^{\frac{1}{2}\left[\mathbb{S}(k_{z_{m,n}}) - \mathbb{S}(\tilde{k}_0\cos\Theta)\right]} e^{\frac{i}{2}\left[\pi - \Omega_m(\tilde{k}_0 r_t \sin\Theta)\right]} \frac{e^{i\tilde{k}_0 R}}{R}. \tag{4}$$
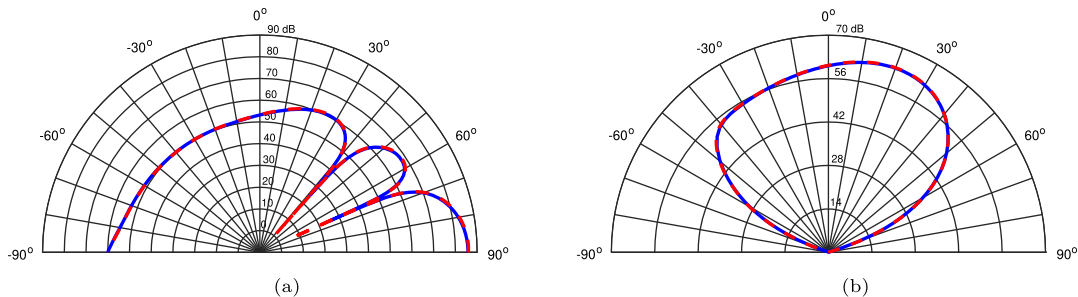
Figure 3. Code comparison at $R = 1$ m distance. The dashed red line is the in-house code and blue is Rienstra's code [15] for the (a) plane wave mode without flow, (b) (8, 0) mode with a $U_0 = 150$ m/s flow moving into the duct.

2.2.1 Code verification

To validate the present code, pressure results produced by it were plotted against results from an existing code developed by Rienstra [15] that was recently made available [16]. Both codes were run under the same conditions and pressure values were produced at the same radial distances. The complex amplitudes $A_{m,n}^+$ as described in Equation (1) used for the in-house code were of unit amplitude for the considered mode (m, n) and zero otherwise. Directivity plots comparing the pressure results around the duct lip for the two codes for the planar mode (0, 0) without flow and for the (8, 0) mode with a flow of 150 m/s are shown in Figure 3.

For every plot included in this paper, the dashed red line gives the results for the in-house analytical code and 90° corresponds to directly in front of the inlet, while for this figure the blue line shows the results for the Rienstra code. There is perfect correspondence between the two codes for all of the modes both with and without flow. The locations of the nodes and the lobe shapes match perfectly, while the pressure levels only differ slightly by a more noticeable drop in the pressure levels at the nodes for the in-house code, which can be explained by different discretizations.

Once the legitimacy of the in-house code was confirmed with an independently produced code, this analytical simulation was used to verify the numerical model described in the following sections.

3 Calculation of the acoustic field

3.1 Acoustic mesh

The considered geometrical configuration was three-dimensional and axisymmetric. Figure 4 shows the full mesh of the fluid surrounding and inside the duct entrance. The narrow wall of the duct is the thin line of white background between the sections of fluid. There is no baffle at the wall, which ends abruptly. Since a wall thickness of zero could not be modeled using this approach, a beveled lip has been used to model the duct inlet.

The air inside the duct and the surrounding air are modeled with a mesh of finite elements (FEs) and this region is also known as the acoustic fluid. Like the analytical version, the numerical model was defined to use the
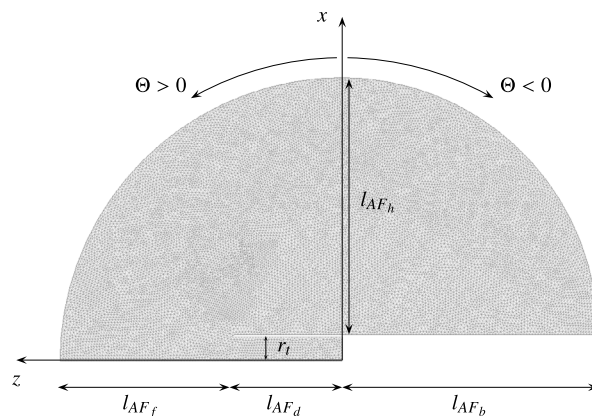

Figure 4. A 2-D slice of the full 3-D axisymmetric acoustic domain.

values listed in Table 1 for a signal moving through a circular three-dimensional duct. The wall thickness r_w was chosen to be much smaller than the duct radius $r_w = r_t/5$ and $r_t/10$. Similarly, the length of the acoustic fluid in front of the duct lip ($l_{AF_f} = 0.694$ m) was chosen to accommodate 10 wavelengths of the acoustic signal. These and other values are included in Table 2 in Section 3.4.

3.2 Acoustic farfield extrapolation

Surrounding this acoustic setup are 180 microphones in a half-circle at an $R = 2$ m radius around the center of the duct inlet. These field points are spaced equidistance apart and measure the acoustic pressure for each propagating mode. Because the field points are located outside of the acoustic fluid an extrapolation technique must be used to project solutions to the wave equation outwards from the finite elements in order to have pressure information at these points. Infinite elements (IEs) were chosen over perfectly matched layers (PMLs) due to the reasons outlined in Section 5.3, and were placed in a one-dimensional line on the far edge of the acoustic fluid (farthest distance from the duct). Due to the geometry of the mesh, this means that there are no IEs directly behind the conduit, which leads to results in this section of the directivity plots being unreliable. To combat this, a mesh with elements behind the duct was considered, however this layout produced unexpected

Table 2. List of considered numerical parameters.

Variable	Symbol	Value
Interpolation order	IO	Linear and Quadratic
Location of input modes	l_{IM}	Line from $(x = 0, y = 0)$ to $(0.085 \text{ m}, 0)$
Wall angle	α	30° and 5°
Wall thickness	r_w	$r_t/5$ and $r_t/10$
Elements per smallest wavelength	N_e	3.4, 6.5, and 12.1
Element shape	ES	Triangular and Quadrangular
Length of acoustic fluid behind l_{IM}	l_{AF_b}	0.906 m and 0.0 m
Duct length in the numerical simulations	l_{AF_d}	0.396 m and 1.302 m
Length of acoustic fluid in front of duct lip	l_{AF_f}	0.604 m
Length of acoustic fluid above the duct wall	l_{AF_h}	0.906 m and 1.302 m

(a) (b)
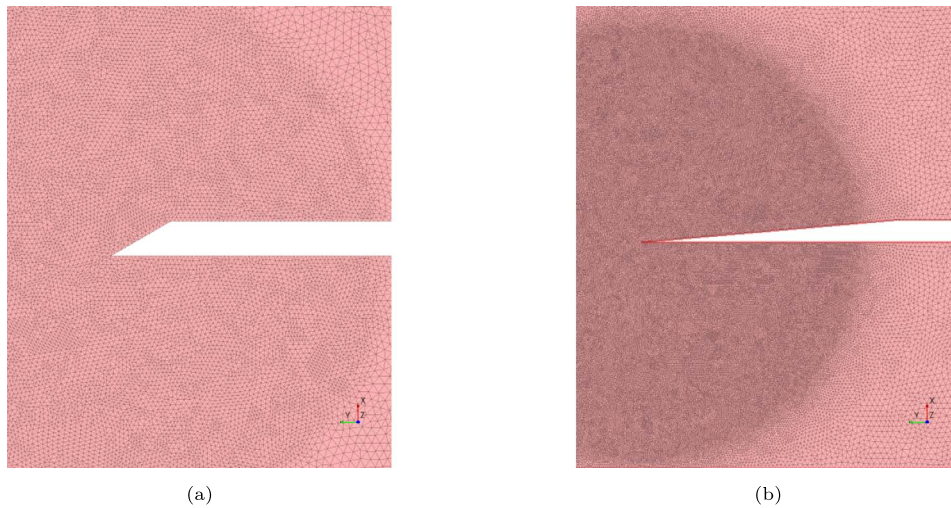
Figure 5. Examples of the tested wall angles for the extra concentrated triangular meshes. Figure 5a shows the 30° angle (defined as the angle between the lowest edge of the duct wall and the angled, forward-facing edge). This angle is rather blunt compared to the 5° angle in Figure 5b.

oscillations behind the duct in the pressure directivity plots. More research should be conducted to determine the source of these oscillations, however this project is only focused on the front half of the plots so this has not been considered here.

3.3 Mean flow solution

Multiple flow fields were considered: uniform flow everywhere, a RANS field with steady flow inside the duct that reduces to no flow at the duct walls and in the far-field, and a potential flow field with steady flow inside the duct that remains high at the duct walls and reduces to no flow in the far-field. Descriptions of illustrations of these fields are compared in Section 6 and Figure 13 for a duct with a bellmouth inlet.

3.4 Numerical code parameters

Multiple numerical meshes were considered, the variables listed in Table 2 were tested, and the differences between the wall angles are illustrated in Figure 5. These

Table 3. List of chosen numerical parameters.

Variable	Configurations
IO	Quadratic
α	30°
r_w	$r_t/10$
N_e	3.4
ES	Triangular
l_{AF_d}	0.396 m

variables were investigated for the following reasons. Linear and quadratic to check run-times and accuracy. Two wall angles were chosen, one to be close to 0° and the other to be significantly larger. The wall thicknesses were selected to be much smaller than the duct radius and still substantially different. Mesh sizes were chosen to test the software recommendations of at least 4 elements per wavelength for quadratic interpolation and 7 elements for linear interpolation. Triangular and quadrangular were also chosen to check run-times and accuracy. Finally, two duct lengths were tested to see if duct length affects mode evanescence as the acoustic signal propagates to the far-field.
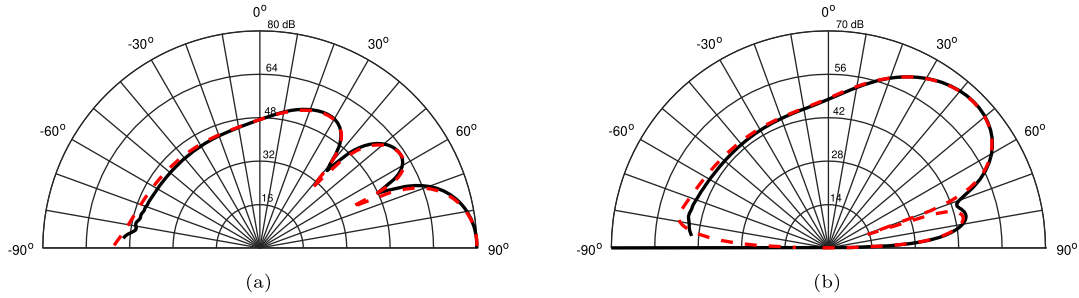
Figure 6. Pressure results comparing the analytical solution (red) to the numerical solution (black) for the plane wave (a) and the (2, 1) mode (b).
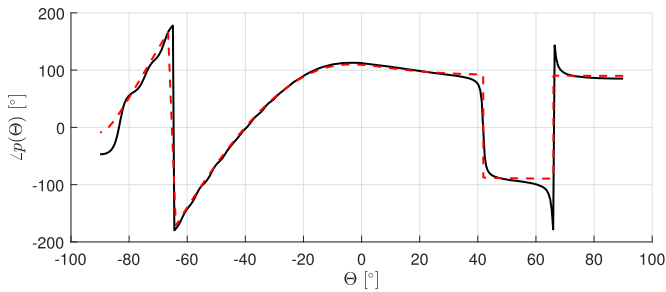

Figure 7. Phase of the acoustic pressure radiated by the mode (0, 0) as a function of the angle Θ. The results are given at $R = 2$ m arc centered at the duct inlet. Analytical results are shown in red and numerical results in black.

Based on these results, the arrangement described in Table 3 was chosen for subsequent simulations. These components were chosen to reduce run-time and data usage as much as possible while still producing accurate results. Wall angle did have an effect on the far-field pressure distribution, and this is discussed in detail in Section 5.4.

4 Results without flow

Both the numerical and the analytical simulations found 15 total modes propagating through the conduit at the frequency of interest and directivity plots of the pressure for all modes were produced and compared. It was found that the numerical results show exact agreement with the analytical solution in the front halves of the plots – the lobes are all in the same locations and the total pressure levels match exactly. The only difference is in the dB dip at each node, which can be explained by the discretization in the FEs.

Two of these plots are given in Figure 6. They show the solutions to the plane wave and (2, 1) modes for the analytical case in red and the numerical case in black. In these plots, 90° corresponds to the axis directly in front of the inlet, and −90° is directly behind it. The only place where there is disagreement between the two result sets is near the −90° mark, and this was expected due to the lack of IEs behind the duct inlet. This close agreement holds true for all modes except two: the (0, 1) and (0, 2) modes both

produced a noticeable difference between the analytical and numerical results in the front of the directivity plots. It was also found to be true for cases with flow, and examples of this can be seen in Figure 8a for the Mach 0.12 case and in Figure 10a for the Mach 0.44 case. This difference is due to the angle of the beveled edge, and an explanation is included in Section 5.4.

The location of the maximum pressure for each mode gives information about its propagation through the conduit. Modes far below cut-off exhibit the highest pressure levels near the axis, while modes that are close to cut-off display the highest pressure levels far from the axis. The lobes exist due to the wave nature of acoustic signals. When sound waves reach the duct opening, part of the signal is transmitted outside of the duct, while part of the signal is reflected back inside. Which part is propagated out depends on the angle of the duct wall, the propagation angle of the signal, and the velocity of the air moving inside the duct.

Because the software does not capture the dips in the pressure graphs, and because this project is more concerned with the values at the lobe maxima, it is not meaningful to compute the overall maximum pressure difference between the numerical and analytical solutions. Instead, the error between the two codes was read by visual comparison of the difference at the location of the highest pressure values. Using this method, it was determined that the maximum difference between the two models is approximately 0.7 dB, which shows that they have good agreement.

Future work will consider in-duct mode detection from far-field measurements. Thus, comparison is also made for the phase distribution of pressure radiated by each mode. Figure 7 shows the phase of the acoustic pressure as a function of the angle around the duct inlet for the analytical and the numerical solutions. It can be seen that both agree quite well. The main discrepancies are close to phase jumps that correspond to pressure dips at the directivity diagram (see Fig. 7). Similar results were found for the other modes.

5 Simulations with flow

Simulations with flow were executed for Mach number values of $M_0 = 0.12$, 0.30, and 0.44 in order to reproduce the typical velocities in the LP3 engine (40 m/s) [20] as well
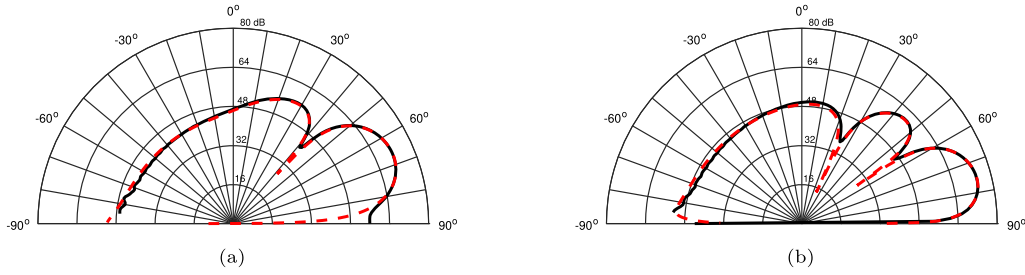
Figure 8. Comparison of pressure results for the $M_0 = 0.12$ simulations between the analytical (red) and numerical (black) simulations for the (0, 1) (a) and the (1, 0) (b) modes.
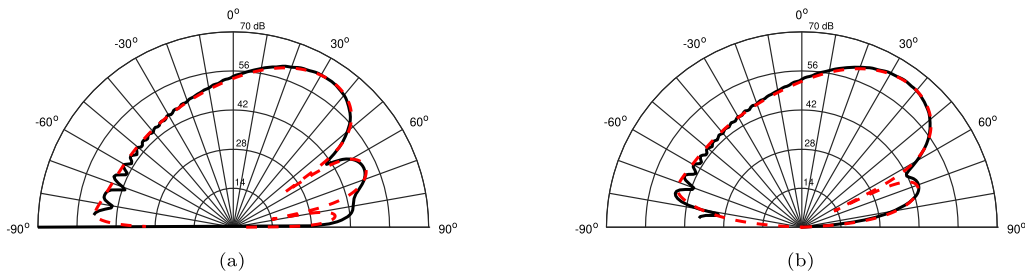

Figure 9. Comparison of pressure results for the $M_0 = 0.30$ simulations between the analytical (red) and numerical (black) simulations for the (1, 2) (a) and (3, 1) (b) modes.
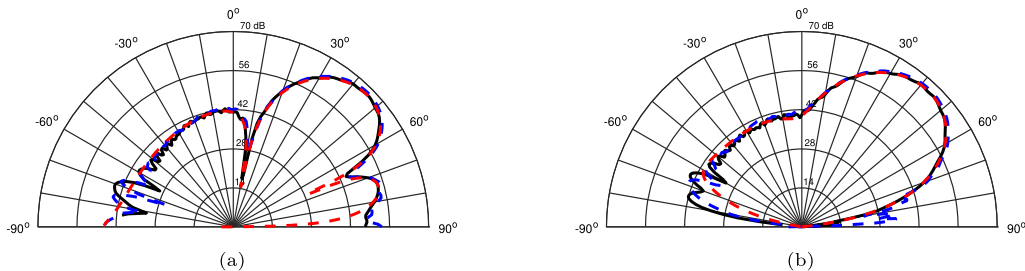

Figure 10. Comparison of pressure results for $M_0 = 0.44$ simulations between the analytical (red) and numerical with IEs (black) and PMLs (blue) for the (0, 2) (a) and (5, 0) (b) modes.

as to test the software's behavior under more extreme conditions (100 and 150 m/s).

The first person to derive an analytical model with flow and diffraction effects was Candel [5, 6], who generated plane wave mode equations for the far-field distribution of acoustical pressure emanating from a cylindrical duct immersed in a constant flow field, defined as having the same velocity inside and outside of the duct. Candel's work then led to Lordi and Homicz' [7, 8] work with higher order modes, which in turn led to Lidoine [12] compiling the solution into the general form explained in Equation (4) in Section 2.1. This equation has been used to produce the analytical results described in the following pages. Both the numerical and the analytical model consider a uniform flow field and use the values defined in Table 1.

5.1 $M_0 = 0.12$ Results

When a $U_0 = 40$ m/s flow field moving into the conduit was defined, the two sets of results showed good agreement with each other. For this velocity, both simulations found 15 total propagating modes. Comparisons of the results are given for the (0, 1) and (1, 0) modes in Figure 8. Like all of the plots included in this section, the red line presents the analytical and the black line the numerical solution, 90° is directly in front of the conduit and −90° is directly behind it, and the pressure was calculated at $R = 2$ m from the duct lip.

For low velocity simulations, the locations of the lobes for both models are in perfect alignment. This holds true across all modes except the (0, 1) and (0, 2) modes, the
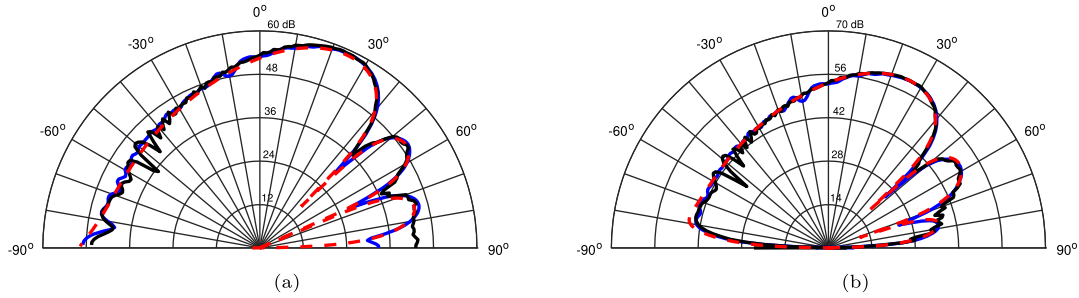
Figure 11. Comparison of analytical (red) and numerical pressure results for $M_0 = 0.44$ simulations for wall with a 30° angle (black) and a 5° angle (blue) for the (0, 3) mode (a) and the (2, 2) mode (b).

reasons for which are described in Section 5.4. The results displayed here include the noticeable section of oscillation directly behind the inlet, which is due to a lack of IEs in that region as can be seen in the mesh shown in Figure 4 and was the same for all models using IEs. This region corresponds to approximately 4° located between −90° and −86° in the graphs.

5.2 $M_0 = 0.30$ Results

Increasing the mean velocity to $U_0 = 100$ m/s led to similar agreement between the analytical and numerical results. This time there were 17 total modes for both simulations, and directivity plots of modes (1, 2) and (3, 1) are given in Figure 9. The only difference at this velocity is that there are small pressure oscillations present in the back approximately 70° of the plots for the numerical simulation.

5.3 $M_0 = 0.44$ Results

A $U_0 = 150$ m/s uniform velocity flow field was also studied. For this velocity, there were 18 total modes propagating through the conduit. Pressure results comparing the analytical and numerical solutions for the (0, 2) and (5, 0) modes are plotted in Figure 10.

The locations of the lobes and pressure levels are in nearly perfect agreement between the analytical (red) and numerical simulations with IEs (black) and PMLs (blue) for the displayed modes. This holds true across all 18 modes, with the exception of directly on the axis for the $(m = 0, n \neq 0)$ modes, see Section 5.4. These plots also show the differences in the solutions produced by the IEs and the PMLs. The primary difference between the two systems is that the PMLs often showed an extra node that was not visible in the analytical solution. This node is included in both of the displayed plots – it occurs at approximately 90° for the (0, 2) mode and at 80° for the (5, 0) mode. It is for this reason that the IEs were chosen for the simulations.

The $U_0 = 150$ m/s numerical simulation produced many oscillations behind the duct. These oscillations were visible as far forward as 10° for some of the modes. In order to verify that these oscillations were not the result of an unrefined mesh, simulations with more than 40 elements per wavelength were conducted and the results remained similar.
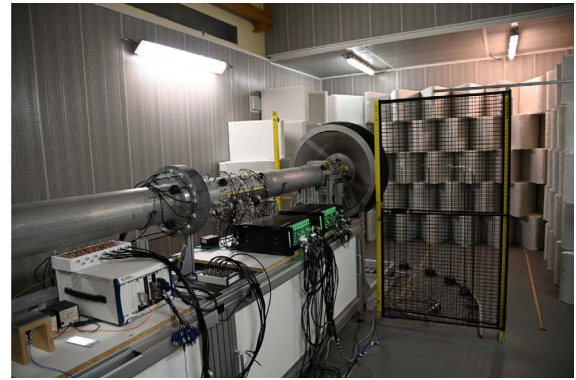

Figure 12. View of the LP3 test rig.

Additional investigation is needed to determine the cause of these oscillations. However, since the oscillations do not affect the pressure results for the front half of the inlet (the section that is of concern for this project), further consideration of this phenomenon will not currently be given.

5.4 Influence of the duct lip geometry

The effect of the wall angle was also tested. For these tests, wall angles of 5° and 30° were considered, with a mesh that was particularly refined around the wall corner. Images of the angles can be seen in Figure 5. Results for the (0, 3) and (2, 2) modes when $M_0 = 0.44$ can be seen in the directivity plots in Figure 11 where they are compared to the analytical solution (see Eq. (4)). A speed of sound $c_0 = 340$ m/s was used.

The angle simulations produced very similar results overall, the only exceptions being at 90° for the $(m = 0, n \neq 0)$ modes, for which the 5° angle simulation better reproduced the front-most nodes found in the analytical simulation. Additionally, behind the conduit the oscillations for the 5° angle results have a noticeably lower amplitude.

6 Applications for the LP3 test rig

The LP3 test rig is an axial, low-speed, ducted fan and a picture of the engine can be seen in Figure 12 [20]. In this picture, the duct is on the left, the fan and turbulence
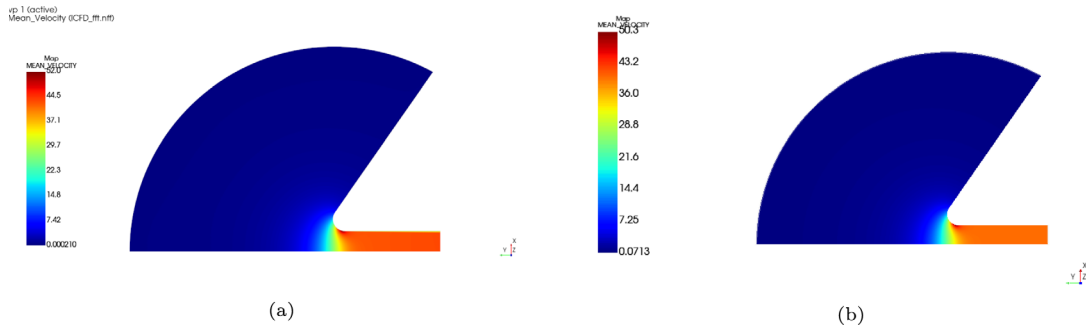
Figure 13. Flow fields for the LP3 simulation with the shape of the bellmouth inlet visible along the right side for the RANS mean velocity profile (a) and the potential velocity profile (b).
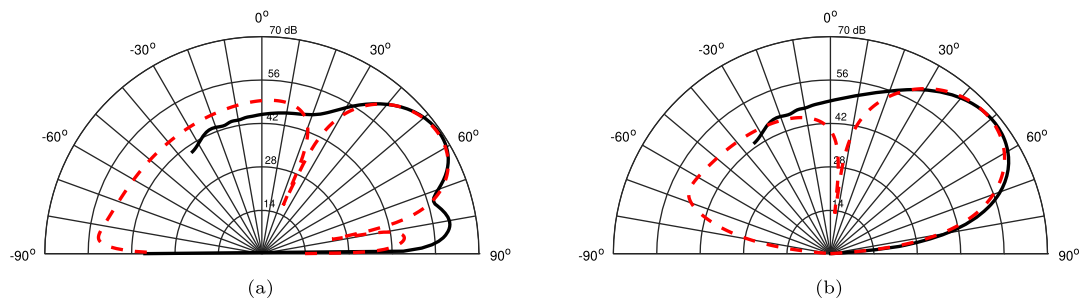

Figure 14. Pressure results comparing the analytical solution for the narrow-wall geometry (red) to the numerical solution for the LP3 geometry without flow (black) for the (1, 1) (a) and the (4, 0) (b) modes.
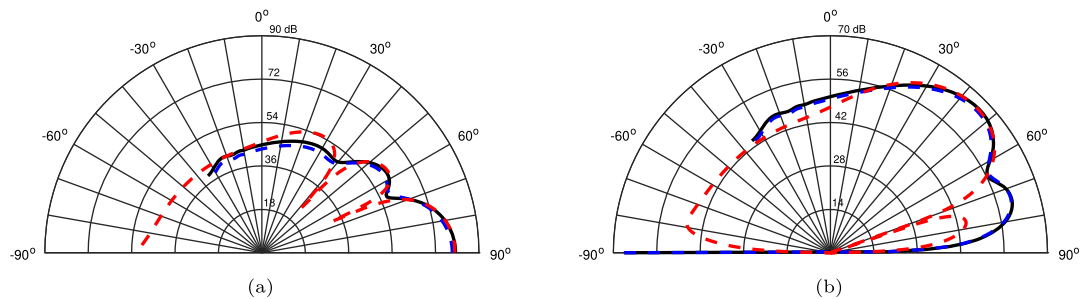

Figure 15. Pressure results comparing the LP3 no flow (black) simulation to the simulation with 40 m/s flow (blue) and the analytical unbaffled duct solution with a 40 m/s uniform flow (red) for the plane wave (a) and the (2, 1) mode (b).

control screen (TCS) are in the center of the image, material for acoustic dampening can be seen along the far wall, and an arc of microphones surrounding the inlet is between the TCS and the dampeners. There is large-angle bellmouth intake skirting at the edge of the duct, the back of which can be seen just before the turbulence control screen. The TCS has been included to homogenize the flow entering the engine duct, and acoustic dampeners line the walls to help reduce reflections that would not be present in real-world applications. There are also multiple recessed microphones lining the inside of the duct, the electrical cables for which can be seen along the side of the conduit. The acoustic sources can be seen as the circular block surrounding the duct circumference near the left hand side of the image.
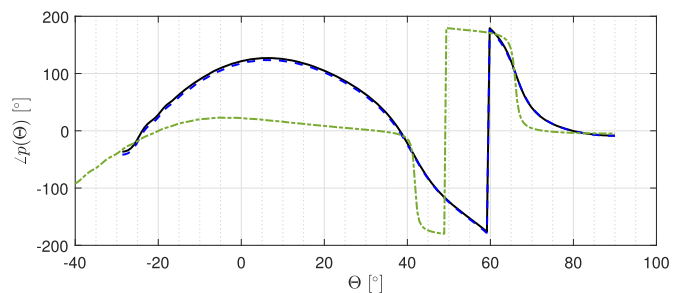

Figure 16. Phase of the acoustic pressure radiated by the mode (0, 0) as a function of the angle Θ. The results are given for the LP3 duct inlet in a static test configuration for a zero mean flow $M_0 = 0$ (black), a $M_0 = 0.12$ flow (dashed blue) and the scarfed lip geometry with $M_0 = 0$ (dashed-dot green).
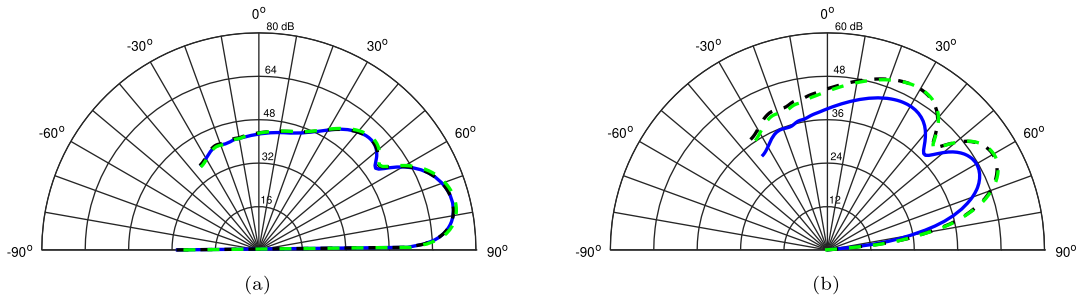
Figure 17. Comparison of the pressure results for the LP3 geometry 40 m/s RANS (blue), potential (black), and uniform (green) flow field pressure results for the $(1, 0)$ mode (a) and the $(4, 1)$ mode (b).

Because simulations of the LP3 rig will be compared to experiment, three different flow fields were considered and compared: a uniform field, a potential field, and a Reynolds-Averaged Navier–Stokes (RANS) field. The potential flow field was considered to obtain a realistic mean flow, and the RANS field was considered to obtain a realistic mean flow with boundary layer effects. Both of these fields are shown in Figure 13, and the primary difference between them is that the RANS field tends to zero in the vicinity of the duct wall. Like the unskirted case considered earlier, these simulations are three-dimensional, axisymmetric, and IEs line the far edge of the acoustic fluid (AF) on the left, beyond which there are microphones placed in the far field. The mode injection site is also the same, the shape of the bellmouth inlet is visible as the edge of the AF, and the finite elements have been arranged with higher density near the inlet to better capture diffraction effects in this location. A speed of sound of 347 m/s was used.

6.1 Impact of the geometry

In order to see how the geometry of the duct affects the far-field pressure, a comparison was made between the analytical solution for the narrow, unbaffled duct wall and the numerical LP3 geometry with the bellmouth intake. Directivity plots for these simulations using the conditions described in Table 1 are given in Figure 14 for the $(1, 1)$ and $(4, 0)$ modes. In these comparisons, the results were not expected to match. These figures were only considered to see to what extent the numerical solution is imperative for predicting the behavior of a realistic, skirted duct.

As these plots illustrate, the numerical simulation for the unbaffled geometry found higher pressure near the axis for the $(m, n \neq 0)$ modes in the front-most lobe and tended not to include any nodes that occur aft of the 30° line. All other nodes are severely reduced in the level of the pressure drop but are still noticeable. This suggests that the addition of bellmouth skirting along the inlet increases the percentage of the acoustic waves transmitted outside of the duct in the upstream direction.

These results are so different, it becomes clear that the geometry of the simulation has a large effect on the external pressure measurements. Therefore, the numerical solution is important for determining the transfer function for unique geometries.
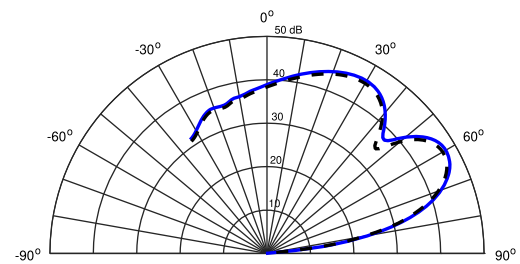

Figure 18. Far-field pressure results for the mode $(4, 1)$ with a refined mesh and the 40 m/s RANS (blue) and potential flow field (black).

6.2 Consideration of flow

The results for the baffled geometry without flow were compared to results for the same geometry with the RANS flow field shown in Figure 13a. Pressure results for the $(0, 0)$ and $(2, 1)$ modes are given in Figure 15, where they are compared to the analytical results for the unbaffled duct. The simulation with flow identified 15 cut-on modes while the simulation without flow identified 14. The extra mode is the $(4, 1)$, and it started propagating due to the change in the variable $\tilde{k}_0$, which lowered the necessary frequency for this to begin propagating as described in Equation (2). It would appear that when flow is added to the new geometry the far-field pressure results are very similar to the results for the same geometry without flow.

The influence of the flow in the phase distribution was evaluated for the LP3 duct inlet geometry. Results are shown in Figure 16 for zero mean flow $M_0 = 0$ and for $M_0 = 0.12$ corresponding to the nominal rotational speed of the LP3 fan. As can be seen, the phase changes very little for the two flow conditions. This result suggests that for an inlet in a static test configuration (see Fig. 13), and for low Mach number, the mean flow has a minor impact on both the amplitude and the phase of the radiated pressure. In contrast to static tests, configurations with an external flow lead to different conclusions due to convective effects. When the Mach number is the same both inside and outside the duct, as is the case of the analytical solution in Equation (4), the phase oscillations increase with the flow due to the term $e^{-iM_0\tilde{k}_0\tilde{z}}$. The numerical solution for the case of a scarfed inlet (see Fig. 4), with $M_0 = 0$ is also added to
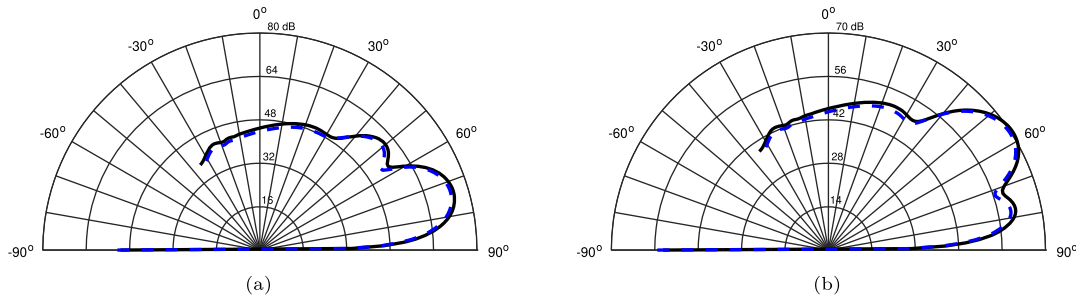
Figure 19. Comparison of the $f = 8$ kHz pressure results for the LP3 geometry without flow (black) and with a RANS 40 m/s flow field (blue) for the (2, 0) (a) and (2, 1) (b) modes.

Figure 16. It can be seen that the phase differences are much greater, suggesting that the inlet geometry has a higher impact than the flow on the transfer functions for static tests. However, it should be kept in mind that the addition of flow will increase the number of cut-on modes and it is crucial to take those into account in the mode identification technique.

Following this, the three different flow types described earlier in this chapter, two of which are displayed in Figure 13, were considered. The velocity field for the potential case is defined as a scalar potential function.

Results for two of the modes from these simulations are included in Figure 17. All three flow fields produced the same far-field pressure results for all of the modes except the (4, 1), which is exhibited in Figure 17b.

For this mode, the results all have the same shape but the RANS simulation found much lower pressure levels than the other two velocity types. Dong and Povinelli [22] found that modes close to cut-off require higher numerical resolution to avoid spurious cut-off, so a more refined mesh was generated and RANS and potential flow simulations were run with the new mesh. The pressure results for the (4, 1) mode with this mesh are given in Figure 18. With the refined mesh, the far-field pressure results for the flow fields begin to converge. The converging results appear to be significantly closer to the results found by the RANS flow simulation, suggesting that this definition is better for determining pressure results for modes close to cut-off. For all other modes the three flow types are effectively interchangeable.

Numerical simulations of the LP3 geometry with a frequency of 8 kHz without flow and with a 40 m/s RANS flow field were also generated, and directivity plots from two modes can be found in Figure 19. These simulations demonstrated that adding flow to the LP3 geometry causes the far-field pressure distribution to lower in decibel level and rotate slightly away from the duct axis. This is the equivalent of a drop in the frequency of the signal moving through the conduit, which is the opposite of what Candel [6] found when working with unbaffled ducts in a uniform flow. Candel's work determined that pressure results from unflanged conduits in a uniform field behave as if the signal frequency increased: higher pressure distributions and a rotation of those distributions towards the duct axis. Because all three field types seemed to produce the same results in the $f = 6$ kHz tests, it is probable that this opposite effect is due specifically to the presence of the bellmouth intake skirting.

7 Conclusion

The directivity pattern of acoustic pressure radiated from duct inlets was found to be highly dependent on the geometry of the inlet. For unbaffled simulations, it was determined that the angle of the leading edge facing the incoming flow has a large effect on the front-most nodes for the ($m = 0$, $n \neq 0$) modes. Additionally, the presence of a bellmouth inlet increases the acoustic radiation in the first lobes near the axis for the (m, $n \neq 0$) modes, decreases radiation at 90° angles from the axis for all modes, and results in the suppression of nodes that occur behind the 30° line. It also reduces the total acoustic pressure drop at all nodes regardless of location or mode number, and reverses how the pressure distributions transform when flow is added.

Different flow definitions have little effect on the simulation outcomes, with the exception of modes near the cut-off frequency. These modes require higher numerical resolution to be found with accurate pressure levels, although low resolution simulations can still identify the shape of the pressure directivity plots for these modes. RANS simulations seem to provide accurate levels under quasi-evanescent conditions, although more testing should be done to verify this. Adding flow changes the angle of maximum signal in the far-field, increasing χ with increasing M_0.

External pressure distributions produced by the in-house analytical code and numerical simulations were observed to have good agreement both with and without flow, although as the flow velocity increased the minor oscillations that were observed in the numerical simulation without flow became more prominent. However, these oscillations all occurred outside of the area of interest, while at the lobe maxima it was found that the greatest difference in the results was never more than approximately 0.7 dB. Other variables did not affect the results so long as the element number per wavelength was sufficient to accommodate the chosen interpolation order and the surface at which modes were imposed was not flush with the duct lip. Rienstra's code was found to have a very good match to the in-house code, never differing by more than 0.5 dB.

Future work will include running experiments on the LP3 testbench [20] described here, and making sure the transfer functions are validated in an experimental setting using a combination of internal and external sensors. Once the functions are fully validated they will be used to perform modal decompositions based on external pressure measurements. These results can later be used to facilitate mode reconstruction exclusively from external pressure measurements on the Phare 2 facility [11, 23].

Conflict of interest

Acknowledgments

References

1. J.W.S. Rayleigh: The Theory of Sound, Second edition (1945) Edition, Vol. 2, Ch. 16. Dover Publications, New York, 1877.
2. H. Levine, J. Schwinger: On the radiation of sound from an unflanged circular pipe. Physical Review 73, 4 (1948) 383–406. https://doi.org/10.1103/physrev.73.383.
3. L.A. Weinstein: The Theory of Diffraction and the Factorization Method (Generalized Wiener-Hopf Technique). Golem Press, 1969.
4. J.M. Tyler, T.G. Sofrin: Axial flow compressor noise studies, in SAE Technical Paper Series. SAE International. 1962. https://doi.org/10.4271/620532.
5. S.M. Candel: Diffraction of a plane wave by a half plane in a subsonic and supersonic medium. Acoustical Society of America (ASA) 54, 4 (1973) 1008–1016. https://doi.org/10.1121/1.1914311.
6. S.M. Candel: Acoustic radiation from the end of two-dimensional duct, effects of uniform flow and duct lining. Elsevier BV 28, 1 (1973) 1–13. https://doi.org/10.1016/s0022-460x(73)80014-8.
7. J. Lordi, G. Homicz, R. Rehm: Effects of finite duct length and blade chord on noise generation by a rotating blade row, in 7th Fluid and Plasma Dynamics Conference, 17–19 June 1974, Palo Alto, CA. American Institute of Aeronautics and Astronautics. 1974. https://doi.org/10.2514/6.1974-555.
8. G. Homicz, J. Lordi: A note on the radiative directivity patterns of duct acoustic modes. Journal of Sound and Vibration 41, 3 (1975) 283–290. https://doi.org/10.1016/S0022-460X(75)80175-1.
9. E.J. Rice, M.F. Heimann, T.G. Sofrin: Modal propagation angles in a cylindrical duct with flow and their relation to sound radiation, in Technical Paper for the Seventeenth Aerospace Sciences Meeting (1979), 15–17 January 1979, New Orleans, LA.
10. A. Snakowska, H. Idczak, B. Bogusz: Modal analysis of the acoustic field radiated from an unflanged cylindrical duct – theory and measurement. Acta Acustica United with Acustica 82 (1996) 201–206.
11. S. Lidoine, H. Batard, S. Troyes, A. Delnevo, M. Roger: Acoustic radiation modelling of aeroengine intake comparison between analytical and numerical methods, in 7th AIAA/CEAS Aeroacoustics Conference and Exhibit, 28–30 May 2001, Maastricht, Netherlands. American Institute of Aeronautics and Astronautics. 2001. https://doi.org/10.2514/6.2001-2140.
12. S. Lidoine: Approches théoriques du problème du rayonnement acoustique par une entrée d'air de turboréacteur: Comparaisons entre différentes méthodes analytiques et numériques, Ph.D. thesis. Ecole Centrale de Lyon, 2002.
13. S. Guerin: Farfield radiation of induct-cutoff pressure waves, in 23rd AIAA/CEAS Aeroacoustics Conference (2019), 5–9 June 2019, Denver, CO. https://doi.org/10.2514/6.2017-4037.
14. A. Pereira, M.C. Jacob: Modal analysis of in-duct fan broadband noise via an iterative bayesian inverse approach. Journal of Sound and Vibration 520 (2022) 116633. https://doi.org/10.1016/j.jsv.2021.116633.
15. S. Rienstra: Acoustic radiation from a semi-infinite annular duct in a uniform subsonic mean flow. Journal of Sound and Vibration 94, 2 (1984) 267–288. https://doi.org/10.1016/s0022-460x(84)80036-x.
16. S.W. Rienstra: Sjoerd W. Rienstra, 2021. https://www.win.tue.nl/~sjoerdr/.
17. A. Pereira, M.C. Jacob: Experimental assessment of in-duct modal content of fan broadband noise via iterative bayesian inverse approach, in 8th Berlin Beamforming Conference (BeBeC) (2020), 2 Mar 2020, Berlin, Germany.
18. S.M. Candel: Analytical studies of some acoustic problems of jet engines, Ph.D. thesis. California Institute of Technology, 1972. https://doi.org/10.7907/E5DD-ZC41.
19. J. Ingenito: Vers une modélisation d'aide à la conception acoustique d'étages de compresseurs centrifuges subsoniques de turbomachines, [Ph.D. thesis]. École Centrale de Lyon, 2010.
20. M. Pestana, A. Pereira, E. Salze, J. Thisse, M. Sanjose, E. Jondeau, P. Souchotte, M. Roger, S. Moreau, J. Regnard, M. Gruber: Aeroacoustics of an axial ducted low mach-number stage: numerical and experimental investigation, in 23rd AIAA/CEAS Aeroacoustics Conference, 5–9 June 2017, Denver, CO. American Institute of Aeronautics and Astronautics. 2017. https://doi.org/10.2514/6.2017-3215.
21. S.W. Rienstra: Fundamentals of Duct Acoustics, Ch.3. Technische Universiteit Eindhoven, 2015.
22. T.Z. Dong, L.A. Povinelli: On computations of duct acoustics with near cut-off frequency, in Second Computational Aeroacoustics (CAA) Workshop on Benchmark Problems NASA-CP-3352 (1997), 1 June 1997, Cleveland, OH, pp. 247–258.
23. R.J. Silcox: Geometry and static flow effects on acoustic radiation from ducts. AIAA Journal 22, 8 (1984) 1087–1093. https://doi.org/10.2514/3.48551.

Appendix

$\mathbb{S}(\xi)$ Function

The $\mathbb{S}(\xi)$ function is defined as,

See the Equation (A.1) *top of the next page*

where the first integral is evaluated in the Cauchy principal value sense and the sign for Ω_m is positive for $m = 0$ and negative otherwise. Both integrals are difficult to evaluate due to the singularity when u equals ξ, however they can

$$S(\xi) = \frac{1}{\pi} \oint_{-\tilde{k}_0}^{\tilde{k}_0} \frac{\Omega_m(r_t\sqrt{\tilde{k}_0^2 - u^2})}{u - \xi} du \pm i\Omega_m(r_t\sqrt{\tilde{k}_0^2 - \xi^2}) + \sum_{s=n_p+1}^{\infty} \ln\left[\frac{\tilde{k}_{z_{m,s}} + \xi}{\tilde{k}_{z_{m,s}} - \xi}\right] - \frac{1}{\pi} \int_{-i\infty}^{i\infty} \frac{\Omega_m(r_t\sqrt{\tilde{k}_0^2 - u^2})}{u - \xi} du, \tag{A.1}$$

$$\frac{1}{\pi} \oint_{-\tilde{k}_0}^{\tilde{k}_0} \frac{\Omega_m(r_t\sqrt{\tilde{k}_0^2 - u^2})}{u - \xi} du = \frac{1}{\pi} \oint_{-\pi/2}^{\pi/2} \tilde{k}_0 r_t \sin\Psi \ln\left| \sin(\Psi) - \frac{\xi}{\tilde{k}_0} \right| \Omega'_m(\tilde{k}_0 r_t \cos\Psi) d\Psi \tag{A.2}$$

be rearranged in order to ease their numerical evaluation. For the first integral, this is done by a change of variables $u = \tilde{k}_0 v$, followed by an integration by parts and finally another change of variables $v = \sin\Psi$, to finally obtain,

See the Equation (A.2) top of the page

For the second integral two variable changes are used as well, first $u = i\tilde{k}_0 x$ and then $x = \xi u/\tilde{k}_0$. After one of the resulting terms cancels out, this leaves,

$$-\frac{1}{\pi} \int_{-i\infty}^{i\infty} \frac{\Omega_m\left(r_t\sqrt{\tilde{k}_0^2 - u^2}\right)}{u - \xi} du$$

$$= +\frac{i}{\pi} \int_{-\infty}^{\infty} \Omega_m\left(r_t\tilde{k}_0 \sqrt{1 + \left(\frac{u\xi}{\tilde{k}_0}\right)^2}\right) \frac{du}{(1 + u^2)}. \tag{A.3}$$